THE JOURNAL OF PHYSICAL CHEMISTRY C

Article

Cite This: J. Phys. Chem. C 2018, 122, 26934−26944

pubs.acs.org/JPCC

Insights on the Alumina−Water Interface Structure by Direct Comparison of Density Functional Simulations with X-ray Reflectivity

Katherine J. Harmon,[†] Ying Chen,[§] Eric J. Bylaska,[∥] Jeffrey G. Catalano,[⊥] Michael J. Bedzyk,[†,‡] John H. Weare,[§] and Paul Fenter*[,#]

[†]Applied Physics Graduate Program and [‡]Materials Science and Engineering Department, Northwestern University, Evanston, Illinois 60208, United States

[§]Chemistry and Biochemistry Department, University of California San Diego, La Jolla, California 92093, United States

[∥]Environmental Molecular Sciences Laboratory, Pacific Northwest National Laboratory, Richland, Washington 99354, United States

[⊥]Department of Earth and Planetary Sciences, Washington University in St. Louis, St. Louis, Missouri 63130, United States

[#]Chemical Sciences and Engineering Division, Argonne National Laboratory, Lemont, Illinois 60439, United States

Supporting Information

ABSTRACT: Density functional theory molecular dynamics (DFT-MD) simulations are frequently used to predict the interfacial structures and dynamical processes at solid−water interfaces in efforts to gain a deeper understanding of these systems. However, the accuracy of these predictions has not been rigorously quantified. Here, direct comparisons between large-scale DFT-MD simulations and high-resolution X-ray reflectivity (XR) measurements of the well-defined Al_2O_3(001)/water interface reveal the relative accuracy of these two methods to describe interfacial structure, a comparison that is enabled by XR's high sensitivity to atomic-scale displacements. The DFT-MD simulated and XR model-fit structures are qualitatively similar, but XR signals calculated directly from the DFT-MD predictions deviate significantly from the experimental data, revealing discrepancies in these two approaches. Differences in the derived interfacial Al_2O_3 relaxation profiles of ∼0.02 Å within the top five layers are significant to XR, but at the limit of the accuracy of DFT. Further differences are found in the surface hydration layer with a simulated average water layer height ∼0.2 Å higher than that observed experimentally. This is outside the accuracy of both XR and DFT and is not improved by the inclusion of a phenomenological correction for hydrogen bonding (e.g., Grimme).

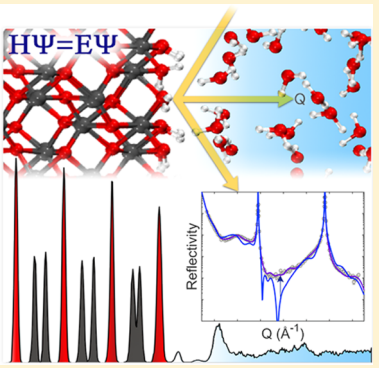

1. INTRODUCTION

Solid−water interfaces are primary sites for a wide range of physiochemical phenomena in natural and technological systems. These include corrosion,[1] catalysis,[2−4] metal ion uptake and mineral reactivity (e.g., sequestration of CO_2 and heavy metals),[5−8] and energy conversion.[9,10] A complete interpretation of how such processes occur requires an accurate and thorough structural and dynamical understanding of the interface region. In particular, a robust understanding of complex hydrogen bond (HB) networks and proton transfer at charged solid−aqueous interfaces would support efforts to describe ion hydration, water dissociation, acid−base behavior, and electrochemical phenomena.

Numerous experimental studies using nonlinear sum-frequency generation (SFG)[11−15] spectroscopy and X-ray reflectivity (XR)[16−23] have explored the structure and dynamics of solid−water interfaces, but with some limitations. SFG is sensitive to the HB network at a solid−water interface, but the interpretation of SFG spectra remains challenging due to the ambiguity in assigning bonds and specific dynamic processes to individual spectral peaks. Meanwhile, high-resolution XR directly probes the atomistic interfacial structure, but the HB network can only be inferred indirectly from XR due to its insensitivity to protons that have a small X-ray scattering cross-section.

First-principles simulations, which explicitly include the HB structure, can provide new insights into interfacial reaction mechanisms and dynamics.[24] Unlike classical molecular dynamics (CMD) simulations based on empirical potentials, density functional theory-MD (DFT-MD) calculations of atomic-level interactions are independent of experimental observations or models and explicitly include ultrafast interfacial reaction dynamics and chemical changes.[25] For example, simulations of infrared and SFG spectra from various levels of theory have revealed the complexity in the number of different bonding orientations that can contribute to

Received: August 31, 2018
Revised: October 16, 2018
Published: October 17, 2018

DOI: 10.1021/acs.jpcc.8b08522
J. Phys. Chem. C 2018, 122, 26934−26944

qualitatively similar spectra.[26−30] However, these calculations of SFG spectra do not quantitatively agree with the SFG data, making it difficult to definitively describe interfacial behavior.

These challenges highlight the need to rigorously validate the accuracy of computational approaches to identify their strengths and weaknesses through direct and quantitative comparisons with well-defined experimental results. Only by thoroughly understanding the successes and shortcomings of simulation tools can we reliably interpret predictions to ascertain a robust picture of HB structure and dynamics at solid−water interfaces.

XR offers a direct test of computational accuracy through the simple and well-defined interactions of X-rays with matter, so that interfacial structures predicted by computational approaches can be compared directly with measured XR intensities. Specular XR directly probes the time-averaged vertical electron density profile at an interface, which can be predicted by computation. Direct comparisons of this kind recently reported for CMD simulations revealed that CMD could accurately predict the interfacial water profile but not the structural displacements of the mineral surface.[31,32] Moreover, CMD calculations cannot predict bond formation and breaking and as a result are not expected to be able to predict chemical reactions. Interfacial structures are of interest for testing the accuracy of DFT-MD due to the loss of translational symmetry across boundaries, which may result in high sensitivity to any discrepancies in the molecular-scale interactions within these low-symmetry structures.

Here, we investigate the ability of DFT-MD based on the Perdew−Burke−Ernzerhof (PBE) functional[33] to accurately predict the structure and dynamics of the α-Al_2O_3(001)/water interface. This is accomplished through comparison of measured high-resolution specular XR data and XR signals calculated directly from the predicted DFT-MD structure. This expands on previous work comparing simulated structures with XR data[31,32] by identifying predicted structural features that contribute to disagreements between simulated XR signals and the XR data. These features are then refined to assess their relative contributions (and importance) to the level of disagreement and discuss the implications for the HB network at the interface.

Experimental XR measurements of the Al_2O_3/water interface structure are well-determined, both for the (001), (012), and (110) crystallographic terminations in contact with fluid water[17−19] and for the Al_2O_3(001) surface termination in humid air.[23] As a result, this system serves as an optimal test case to benchmark the accuracy of DFT-MD predictions of complex oxide/water interfaces. We selected the widely used PBE96 functional[27,29,34] for the first test of this theory−experiment comparison as it reasonably predicts bulk water behavior at a relatively low computational cost compared to hybrid functionals,[35] which are impractical for use in large simulations. Previous work has demonstrated that PBE can accurately reproduce the bulk alumina geometric and electronic properties, whereas the hybrid functional PBE0[36] performs slightly worse with respect to bulk alumina at significant added cost[37] and only offers minimal improvement to the structure and dynamics of bulk water.[35,37] The Al_2O_3/water interface has also previously been explored using different levels of computation from all-atom MD[38] to DFT-MD, including BLYP[39,40] and PBE,[29] but these studies have not quantitatively assessed the accuracy of the predicted structures with respect to experimental observations to the level presented here.

We also explore the sensitivity of the predicted structure with inclusion of the Grimme2 dispersion correction[41,42] with PBE to test the ability of Grimme2 to account for long-range van der Waals interactions not included in semilocal PBE. Ultimately, a quantitative assessment of predicted structures by various functionals and computational tools can help guide us to the level of theory needed to accurately represent oxide/water systems from which we can glean accurate physiochemical behavior.

2. METHODS

2.1. Computational Methods. Simulations were performed using the pseudopotential plane-wave program NWPW[43,44] contained in the NWChem computational chemistry package.[45] Two separate calculations were carried out using the PBE96[37] exchange−correlation functional, one with and one without the Grimme2[41,42] correction. In both cases, the structural properties of a perfect bulk alumina crystal were first optimized using a 2 × 2 × 1 Monkhorst−Pack Brillouin zone sampling.[46] The valence electron interactions were approximated using generalized norm-conserving Hamann pseudopotentials[47] generated using PBE96 in a separable form suggested by Kleinman and Bylander[48,49] (see Supporting Information for core radii). The electronic wavefunctions were expanded using a plane-wave basis with periodic boundary conditions with a wavefunction cutoff energy of 100 Ry and a density cutoff energy of 200 Ry were based on previous studies.[50] With PBE96, this gave bulk alumina lattice parameters of $a = b = 4.767$ Å, $c = 12.999$ Å, $\alpha = \beta = 90°$, and $\gamma = 120°$, which are within 0.2% of experimental results ($a = b = 4.757$ Å, $c = 12.998$ Å)[51] and verify the applicability of PBE96 to this system. Relaxing the unit cell upon addition of the Grimme2 correction gave lattice parameters of $a = b = 4.746$ Å, $c = 12.911$ Å (0.7% smaller than the experimental result) and $\alpha = \beta = 90°$ and $\gamma = 120°$.

DFT-MD simulations of the solvated Al_2O_3(001)/water system were performed in a periodic unit cell with dimensions $a = b = 9.534$ Å and $c = 45.150$ Å, $\alpha = \beta = 90°$ and $\gamma = 120°$ (Figure 1a) at the Γ-point of the Brillioun zone using the Car−Parrinello method.[24,52] The size of the cell and number of water molecules were chosen specifically to capture the known extent of changes to the alumina surface structure and the modulation of the interfacial water.[19,53] Consequently, the alumina surface was modeled as a 12-layer 2 × 2 slab with deuterated surface oxygens (to allow for larger MD time steps; i.e., $Al_{88}O_{144}D_{24}$, 1086 valence electrons). Sixty-four D_2O (512 valence electrons) were placed in the vacuum between alumina slabs in the periodic cell (for a water density ∼1 g/cm^3). The requirement of sampling configuration space over these 1598 valence electron prohibited the use of hybrid functionals. The initial interfacial hydration structures were generated using a mixed DFT-MD/molecular mechanical (DFT-MD/MM) model in which the positions of the slab were fixed and the water molecules were modeled using the extended simple point charge model interaction potential. This DFT-MD/MM model has been shown to produce excellent agreement with experimental data for the hydration structure of charged ions in solution (i.e., Zn^{2+} aqua ion).[54] In the calculations reported here, the initial DFT-MD/MM structures were equilibrated by DFT-MD for 1.5 ps during which time the potential and kinetic energies stabilized. Trajectory snapshots were then

DOI: 10.1021/acs.jpcc.8b08522
J. Phys. Chem. C 2018, 122, 26934−26944

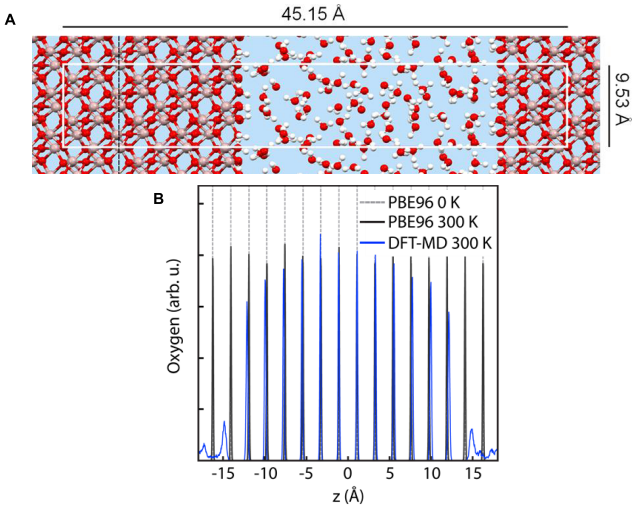

Figure 1. (A) Snapshot of the $Al_2O_3(001)$/water system from the PBE-based DFT-MD simulation is shown with the supercell perpendicular to the alumina (001) surface indicated by the white box. The vertical dashed line (at left) coincides with the alumina slab center at $z = 0$ in (B). The O atoms are red, Al atoms are pink, and H atoms are white. (B) An overlay of O atom positions in alumina from the DFT calculations of the bulk alumina structure at 0 K and at 300 K and from the hydrated DFT-MD alumina slab reveals a small but significant expansion of O spacing upon solvation. Peaks at ±15 Å in the DFT-MD plot (blue) are the start of the water profile.

collected every 1.2 fs for 10 ps during which time the simulation did not evolve significantly. These simulations were carried out in the presence of Nosé–Hoover thermostats[55−57] with a time step of 0.12 fs and fictitious mass of 750 au. The temperature and period of the ionic and electronic thermostats were set to 300 K and 1200 au, respectively.

We note that only a small expansion of the slab and small changes near the water–slab interface were observed during equilibration (Figure 1b). A comparison of the time-averaged oxygen atom structure along the alumina (001) direction from the PBE96-based DFT-MD and the initial PBE96 DFT shows that the O–O distances near the slab center are similar to those of the bulk PBE96 calculation and expand slightly near the surface upon solvation.

2.2. Experimental Methods. XR data were collected at beamline 33-ID-D at the Advanced Photon Source at a photon energy of 12 keV. A single crystal $Al_2O_3(001)$ substrate was rinsed, annealed, and mounted in a thin-film cell in ultrapure deionized water, and XR data were acquired according to the procedures previously described.[19]

The experimental $Al_2O_3(001)$/water interface structure along the (001) plane normal, $\rho(z)$, was determined by direct comparison of measured specular XR data to calculated XR intensities based on atomistic models of the $Al_2O_3(001)$/water interface. These models consist of a semi-infinite known, fixed bulk alumina structure with lattice constant 12.998 Å, five layers of Al_2O_3 interface (e.g., repeating layers of Al, Al, and three O planes above the bulk structure), an adsorbed water layer, and a layered bulk water model (see previous XR studies of the $Al_2O_3(001)$/water interface[19,23] for more detailed discussion of the models used). Each atomic layer, i, in the system was modeled as a Gaussian defined by an atomic number, Z_i, position, z_i, vibrational amplitude, u_i, and coverage, Θ_i

$$\rho(z) = \sum_i \frac{Z_i \Theta_i}{\sqrt{2\pi u_i^2}} e^{-(z-z_i)^2/2u_i^2} \quad (1)$$

The position, vibrational amplitude, and coverage for each of the interfacial alumina layers and the adsorbed water layer were optimized through an iterative nonlinear least-squares fitting procedure. The model for the layered interfacial water[59] above the first adsorbed water layer consists of a series of Gaussians with fixed layer spacing and occupations and with the vibrational amplitude increasing away from the alumina slab to achieve the known bulk density for water. In this case, the fitting parameters are the height of the first Gaussian above the alumina surface, d_0, distance between adjacent Gaussian peaks, d_w, width of the first Gaussian, u_0, and change in u moving away from the surface, $\bar{u}$. The nth layer in the layered water model is described by

$$z_n = d_0 + n \cdot d_w$$
$$u_n = \sqrt{u_0^2 + n\,\bar{u}^2}$$
$$\Theta_w = \frac{A_{UC} \cdot d_w}{V_w} \quad (2)$$

Within this model, the water layer coverage, Θ_w, depends on the alumina (001) in-plane unit cell area, A_{UC}, d_w, and the volume of a water molecule, V_w, such that each layer in the layered water has the density of bulk water (≈0.33 $e^-/Å^3$). Finally, an alumina surface roughness, $B < 1$, was determined using the Robinson model[60] as

$$B(Q) = \frac{1 - \beta^2}{1 + \beta^2 - 2\beta \cos(Qc)} \quad (3)$$

where β is the fitting parameter, c is the alumina (001) lattice constant, and Q is the momentum transfer, $Q = 4\pi \sin(\theta)/\lambda$. λ is the incident X-ray wavelength and θ the incident angle. Surface roughness is manifested as a reduction in the scattered intensity primarily between the substrate alumina Bragg peaks as compared to a perfectly smooth alumina surface.

In the nonlinear least-squares fitting process, the XR intensity was calculated from the model via Fourier transform of $\rho(z)$ as

$$R(Q) = B(Q)\left(\frac{4\pi r_e}{A_{UC} Q}\right)^2 \left| \int \rho(z)\, e^{iQz}\, dz \right| \quad (4)$$

where r_e is the classical electron radius. The quality of agreement between the calculated XR, $R_{calc}(Q)$, and the experimental XR data, $R(Q)$, is given by

$$\chi^2 = \frac{1}{N} \sum_Q \left(\frac{R(Q) - R_{calc}(Q)}{\sigma(Q)} \right)^2 \quad (5)$$

where N is the number of data points and σ is the experimental error at Q. The model fitting parameters described above were iterated until χ^2 converged. Ultimately, a best fit structure with $\chi^2 = 1.54$ (Figure 2) was obtained (for reference, an ideal fit has $\chi^2 = 1$). The surface roughness parameter was $\beta = 0.30 \pm 0.01$ for the best fit structure.

2.3. Computation vs Experiment Comparison. Predicted atomistic electron density profiles along the $Al_2O_3(001)$ direction were calculated from the DFT-MD simulations, providing a pathway for direct comparison with XR data using

DOI: 10.1021/acs.jpcc.8b08522
J. Phys. Chem. C 2018, 122, 26934−26944

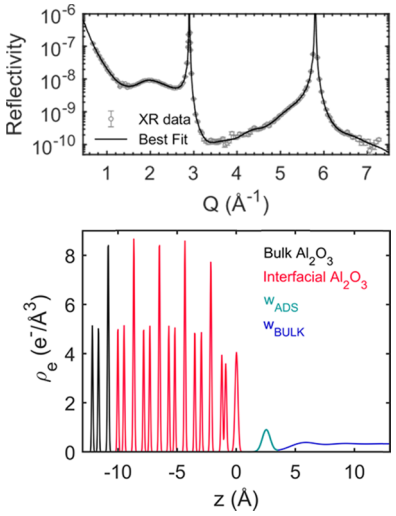

Figure 2. Best fit to the XR data gives χ^2 = 1.54 (top) and corresponds to an electron density profile (bottom) with an interfacial layer of alumina demonstrating surface relaxations, a well-defined adsorbed water layer, w_{ads}, and a layered bulk water model, w_{bulk}, with rapidly decaying oscillations.

eq 4. The number density profile, $n(z) = \sum_i n_i$, from each DFT-MD supercell simulation was determined as the time- and laterally averaged (in the *xy*-plane) atomic structure for each element *i* with a vertical bin size b = 0.033 Å. Electron density profiles were calculated as $\rho(z) = \sum_i Z_i n_i$, where Z_i is the atomic number of the *i*th element. Quantitative comparisons between DFT-MD and the experimental XR intensities were then performed in two ways. In the first method, a section of the DFT-MD electron density profile (from the center of one alumina slab to the center of the water region between slabs, Figure S1) was extracted and imbedded between the known bulk structures of the alumina substrate and the water (the latter in the form of an error function profile, Figure 3a top). The extracted portion of the DFT-MD water included both interfacial and bulk water as the DFT-MD achieved bulk water density for $z \geq 10$. The semi-infinite error function water

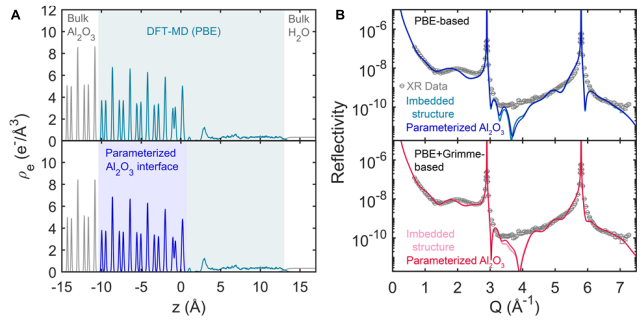

Figure 3. (A) PBE-based DFT-MD electron density profile was imbedded (teal) between bulk alumina and bulk water structures (gray) with both the predicted alumina and predicted water structures directly included (top) and with a parameterized DFT-MD alumina structure (bottom, blue). The same was done for the PBE + Grimme-based DFT-MD (not shown). (B) XR curves calculated from the incorporated DFT-MD structures are in close agreement: (top) χ^2 = 219.2 for the fully imbedded PBE-based structure (teal) and χ^2 = 223.3 parameterized (blue); (bottom) χ^2 = 122.0 for the fully imbedded PBE + Grimme-based structure (pink) and χ^2 = 128.4 parameterized (red).

profile was chosen to prevent any extrinsic signals associated with a discontinuity between the simulated and modeled water profiles. In the second method of direct comparison, the simulated electron density profiles were parameterized as a set of Gaussian functions described by the same parameters used in the model-dependent XR data analysis (eq 1, Figure S2, Table S1) and incorporated into the parameter space of the XR data fitting framework (Figure 3a bottom). Simulated XR signals were calculated from the fully embedded DFT-MD elemental density profiles and partly parameterized profiles and then compared directly to the XR data using the χ^2 quality of agreement (eq 5). The extrinsic roughness parameter (eq 3) was included and optimized for all DFT-MD−XR comparisons, including the initial fit and all optimization steps. This removed any contribution to a mismatch between the calculated and experimental XR data caused by the finite surface roughness that is inherent to these XR data. Agreement between XR signals calculated from these structures (Figure 3b) shows that the parameterization provided a representation of the simulation equivalent to that in the embedding process. However, it is apparent that the calculated signals deviate significantly from the experimental data. This will be analyzed in detail below.

These two approaches for comparing predicted structures to XR data provide consistent quantitative results, but the second approach is more useful to distinguish the source and significance of any discrepancies between DFT-MD and experiment. As can be seen in Figure 3b, there are minor differences in the predicted XR signals when incorporating the simulated structures. This can be attributed to the simplifying assumptions in the calculation of the parameterized structure. For example, the assumption that each interfacial water layer can be described by a Gaussian function may not be valid. Additionally, we have assumed that the simulated interfacial vibrational amplitudes in the alumina substrate decay to the bulk values with an exponential decay (see Supporting Information), which did not perfectly describe the predicted behavior. Subtle differences in peak heights between the two alumina electron density profiles in Figure 3a are a direct result of these differences in the interfacial vibrational amplitudes. Nevertheless, the differences are minor as can be seen in the XR comparison of embedded and parameterized structures (Figure 3b). Further details of the DFT-MD alumina parameterization and methodology for direct comparison to XR data can be found in the Supporting Information and previous studies.[31,61]

3. RESULTS

3.1. Comparison of Simulated and Measured Structures. A comparison of the interfacial DFT-MD and XR best fit electron densities shows that the DFT-MD simulations with and without the Grimme correction both capture many of the features observed in the experimental structure (Figure 4a). The overall density profiles are visually similar, and both experimental and computational approaches find that the vibrational amplitudes, *u*, and interfacial atom locations deviate from the expected bulklike values, especially in the topmost layer (Figure 4b,c). Therefore, the DFT-MD prediction provides qualitatively accurate insights to the structure of this interface. Yet, it is also evident that the XR signals calculated from the DFT-MD simulations are in quantitatively poor agreement with the experimental data with χ^2 = 223 for the PBE-based simulation and χ^2 = 128 for

DOI: 10.1021/acs.jpcc.8b08522
J. Phys. Chem. C 2018, 122, 26934−26944

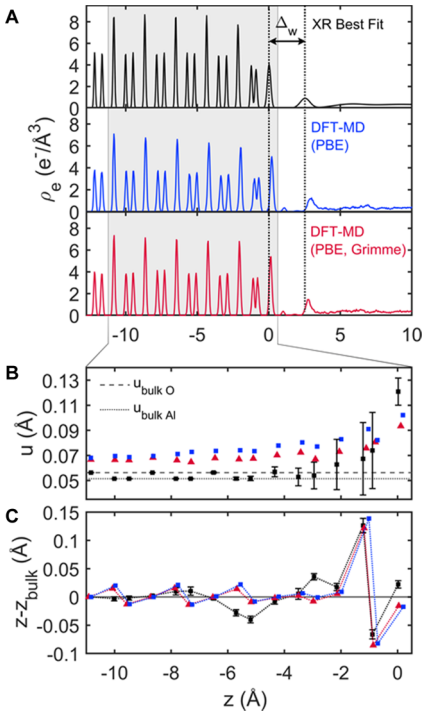

Figure 4. (A) Best fit structure to the XR data (black, top) qualitatively agrees with the DFT-MD predictions using the PBE (blue, middle) and PBE + Grimme (red, bottom) functionals. The dotted vertical lines indicate the location of the XR best fit alumina surface oxygen position and first hydration layer at Δ_w above the surface. (B) Vibrational amplitudes in the DFT-MD alumina slabs are overestimated relative to those in the best fit and compared to expected bulk values for O atoms (dashed line) and Al atoms (dotted line). (C) Displacements for each atomic layer relative to its expected bulk position indicate surface relaxations four layers deep in the best fit structure but only in the topmost layer in the DFT-MD structures.

the PBE + Grimme-based simulation (Figure 3). These discrepancies have multiples sources, as discussed below.

The first source of differences in calculated XR signals is due to the bulk Al_2O_3 structure that is predicted by the DFT-MD simulations, to which XR is highly sensitive.[62] As previously stated, the center of each alumina slab was taken to be bulklike due to the observation from the XR best fit that the alumina surface relaxation was negligible below the fifth alumina layer (Figure 4c). The "effective bulk" DFT-MD lattice constant for each simulation was calculated as 6 times the interoxygen spacing at the slab center. For the PBE-based simulation, the effective alumina (001) lattice constant was 13.26 Å, ~2% larger than the known value (12.998 Å).[51] The DFT-MD calculation based on PBE + Grimme performed somewhat better, giving an effective bulk lattice constant of 13.17 Å (1.3% larger than the known value), but it did not sufficiently improve the predicted structure. These can be compared to the more accurate value obtained in the calculation of the bulk alumina layer spacing by DFT (PBE), which differed from the known structure by only 0.2%. This level of agreement between the "effective" lattice constants from the alumina slab calculations and the true bulk lattice constant from the PBE calculation suggests that the large 12-layered DFT-MD slab may not be fully converged. It is also apparent that both DFT-MD electron density profiles (PBE-based and PBE + Grimme-based) have density peaks that are broader and shorter than those in the XR best fit model. This indicates that the vibrational amplitudes, u, in the DFT-MD simulations are larger than expected (Figure 4b). PBE-based DFT-MD overestimates u of atoms in the alumina surface by an average of 0.016 Å or 26%. PBE + Grimme-based DFT-MD again performs slightly better, overestimating the vibrational amplitudes by 0.01 Å, roughly 16%.

A second source of discrepancies is in the predicted alumina interfacial structure. This is characterized as a relaxation profile that quantifies the displacement of the interfacial atom locations with respect to their bulklike positions. The DFT-MD alumina surface relaxation profiles reveal significant vertical displacements only in the first Al_2O_3 layer. This differs from the XR best fit result, which includes a non-negligible oscillatory relaxation profile that extends four layers into the alumina surface (Figure 2c). The root-mean-square (rms) difference between the PBE-based simulation and the XR best fit alumina surface atom positions, after bulk lattice scaling, is 0.024 Å. The PBE + Grimme-based DFT-MD performs similarly, deviating from the XR best fit relaxation profile by 0.023 Å. These differences in atom positions are approximately the same magnitude as discrepancies in the bulk alumina lattice constant determined by the DFT calculations.

A third discrepancy is observed in the predicted interfacial water structure. This can be characterized by the height of the first adsorbed water layer above the alumina surface, Δ_w (Figure 2a), measured as the vertical O−O separation between the alumina surface oxygen and the nearest water oxygen. This value is 2.729 ± 0.008 Å in the PBE-based simulation and 2.628 ± 0.005 Å in the PBE + Grimme-based simulation. However, the XR best fit was described by Δ_w = 2.512 ± 0.014 Å.

These structural differences between the XR best fit model and the predictions by DFT-MD are summarized in Table 1.

Table 1. Structure Characteristic Lengths (Å)

feature	XR	PBE	PBE + Grimme
c^a	12.998	13.260	13.166
$\langle u \rangle^b$	0.061(3)	0.077(6)	0.071(3)
$\Delta z_{rms}{}^c$	0.041	0.042	0.038
$\delta_{rms}{}^d$		0.0236	0.0227
$\Delta_w{}^e$	2.519(14)	2.729(8)	2.628(5)

[a]Al_2O_3(001) lattice constant. [b]Mean vibrational amplitude within the top five layers of Al_2O_3 (uncertainties in parentheses). [c]rms displacement from the expected bulk atom positions in the top five Al_2O_3 layers. [d]rms deviation from XR best fit after bulk corrections. [e]Height of first adsorbed water layer above Al_2O_3. Uncertainties for simulated structures are those from Gaussian fits of the predicted electron density profiles.

In the following sections (Sections 3.2 through 3.4), the relative significance of the observed differences between simulations and XR data is assessed in a step-by-step process using the calculated and observed intensities as a measure of accuracy (Figure 5).

3.2. Sensitivity to Bulk Alumina Structure. First, the DFT-MD bulk Al_2O_3 lattice constant was scaled from the DFT-MD predicted values to the experimentally observed value (Figure 5i,ii). This improved the quality of fit of the calculated XR from the PBE-based simulation from χ^2 = 223 to 91 (Figure 5a,i,ii) and for the PBE + Grimme-based simulation from χ^2 = 128 to 61 (Figure 5b,i,ii). Most of the χ^2 reduction originates near the alumina Bragg peaks at momentum

DOI: 10.1021/acs.jpcc.8b08522
J. Phys. Chem. C 2018, 122, 26934−26944

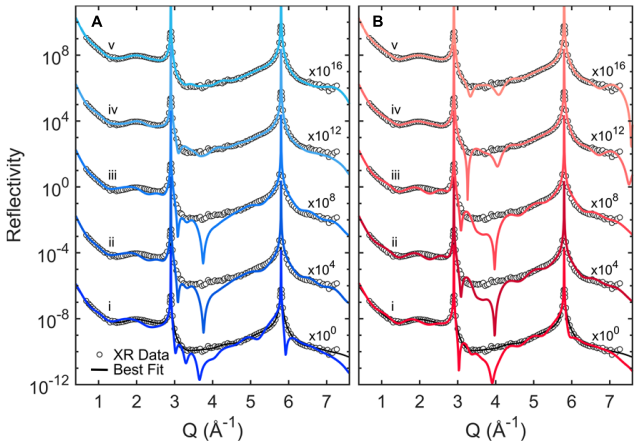

Figure 5. Series of XR curves (i–v) calculated from DFT-MD-based structures show improvements with each optimization step that was performed on (A) the PBE-based prediction and (B) the PBE + Grimme-based prediction. The optimizations are the same for both simulations: (i) initial prediction, χ_A^2 = 223 and χ_B^2 = 128; (ii) scaled lattice constant, χ_A^2 = 91 and χ_B^2 = 60; (iii) offset vibrational amplitudes, χ_A^2 = 94 and χ_B^2 = 63; (iv) optimized alumina surface relaxation, χ_A^2 = 22 and χ_B^2 = 11; and (v) optimized water height, χ_A^2 = 6 and χ_B^2 = 8. Calculated intensities are compared to the XR best fit (χ^2 = 1.54, black line) and XR data (gray circles) for reference and offset as indicated for clarity. See Supporting Information Figure S4 for residuals.

transfers Q = 2.9 and 5.8 Å^{-1}. Thus, the inaccuracy of the bulk alumina lattice constant in the DFT-MD supercells, though small, contributes significantly to the disagreement with XR data.

Next, we assessed the significance of differences in the simulated and measured vibrational amplitudes, *u*, of each atom in the alumina slab. The simulated vibrational amplitudes were offset by the excess seen at the bulk alumina (i.e., at heights $z \leq 10$ Å below the alumina surface) so that *u* decays to the known bulk values (Figures 5iii and S3). This had only a small effect on the quality of fit of the calculated XR intensities from both simulations (PBE-based χ^2 = 94 Figure 5a,iii, and PBE + Grimme-based χ^2 = 60 Figure 5b,iii). Together with the large derived uncertainties in *u* in the XR best fit, this indicates a relative insensitivity of XR to small changes in interfacial vibrational amplitudes. These improvements are associated solely with the differences between the true bulk alumina and the alumina structure at the center of the 12-layer DFT-MD simulation slab. Yet, the XR signals (Figure 5iii) still differ significantly from the measured XR data. Therefore, the remaining discrepancies are due to differences between the predicted and measured interfacial structures, including the alumina surface relaxation and interfacial water structure.

3.3. Sensitivity to Alumina Interfacial Structure. The interfacial alumina atom positions in the parameterized DFT-MD interface were refined to the XR data while keeping the interfacial water profile height fixed at the DFT-MD-predicted values (Figure 5iv). This improved the agreement of the calculated XR intensities with the XR data to χ^2 = 22 and 11 for the PBE-based and PBE + Grimme-based simulations, respectively (Figure 5a-iv and 5b-iv, respectively). This change (nearly 80% improvement for both simulations) substantially reduced oscillations in the XR calculated from the DFT-MD results (i.e., near Q ≈ 2.5 Å^{-1}), indicating that the calculated interference of X-rays scattered from atoms in the predicted structure was inconsistent with the behavior defined by the XR data. The interfacial relaxation of the DFT-MD structure differed from the XR best fit structure by only ~0.02 Å on average in both predicted structures (Table 1), highlighting the extreme sensitivity of high-resolution XR measurements to sub-angstrom displacements in the interface region. Additionally, an oscillatory relaxation pattern similar to the one found in the XR best fit emerged following this refinement (Figure 6),

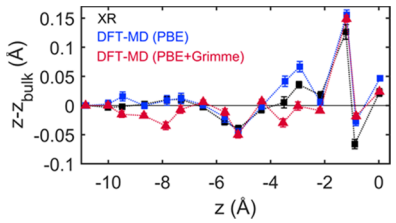

Figure 6. Optimized alumina relaxation behaviors obtained with a fixed water profile height as defined by DFT-MD. These displacement fields had rms differences from the XR best fit relaxation of 0.0192 Å for the PBE-based simulation (blue) and 0.0245 Å for the PBE + Grimme-based simulation (red).

suggesting that this pattern is necessary for agreement with the XR data despite being absent from the simulated structure. Although these alumina relaxation patterns are more similar to that obtained by the XR best fit, the residual discrepancies between the predicted XR signals and the XR data indicate that there remain additional inconsistencies with respect to other features of the DFT-MD-based interfacial structure.

3.4. Sensitivity to Interfacial Water Structure. Next, we assessed the contribution of the interfacial water structure to the remaining discrepancies between the DFT-MD predictions and the XR data. The water profiles are characterized by the height Δ_w, coverage, and vibrational amplitude of the first adsorbed water layer as well as the shape of the subsequent weakly modulated water layer at $z > 3$ Å. We tested the sensitivity of the calculated XR to the first water layer height, Δ_w, by rigidly displacing the DFT-MD water profile closer to the alumina surface while allowing all other aspects of the alumina interfacial structure to relax. This resulted in an optimal height of 2.53 ± 0.01 Å for both simulated water structures, consistent to the distance found in the XR best fit (Figure 7a). Moreover, as a result of the water height adjustment, the optimized alumina atom positions further converged toward the oscillatory relaxation pattern observed in the experimental best fit model (Figure S5; compare to Figure 6). The optimized structures gave calculated XR signals with χ^2 = 5.9 and 7.6 for the PBE-predicted and PBE + Grimme-predicted water structures, respectively (Figure 5a–v and 5b–v, respectively) and visually reproduce most of the features in the experimental XR data. However, intensity oscillations can still be seen in the PBE + Grimme-based XR at Q ≈ 3–4 Å^{-1}. This, and the observation that the quality of agreement is still worse than that obtained by a model fit, indicates that these residual discrepancies are due to the specific modulation of the interfacial water density in the predicted water structure.

These results demonstrate the sensitivity of the XR data to the interfacial water structure, specifically the height of the water profile. More generally, the XR data are also sensitive to the shape of the interfacial water distribution. For example, in comparing the simulated and measured profiles, we find that residual inconsistencies between the predicted and best fit

DOI: 10.1021/acs.jpcc.8b08522
J. Phys. Chem. C 2018, 122, 26934–26944

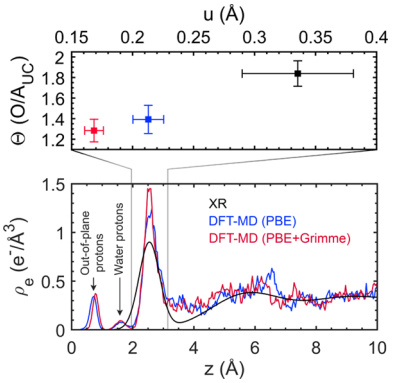

Figure 7. Heights of the first adsorbed water layer of the DFT-MD predicted structures (PBE in blue, PBE + Grimme in red) agree with that of the XR best fit (black) following optimization. Significant differences remain in vibrational amplitudes, u, and coverages, Θ, in the first adsorbed water layer and changes in the water density near 3−4 Å. The density associated with protons is indicated (i.e., those terminating the alumina surface and those in water) but is not probed in the XR result. Uncertainties in the DFT-MD coverage and width are from Gaussian fits to the electron density profiles.

water structures include the coverage and vibrational amplitude of water molecules in the first adsorbed water layer at ∼2.5 Å above the alumina (Figure 7 and Table S1). The PBE-based DFT-MD predicted a coverage of 1.4 O/A_{UC} and width of 0.21 Å, whereas the PBE + Grimme-based DFT-MD predicted a coverage of 1.28 O/A_{UC} and width of 0.17 Å. These values are underestimated relative to those in the XR best fit (1.84 ± 0.12 O/A_{UC} and 0.34 ± 0.06 Å). The same behavior of underestimating hydration layer vibrational width was observed for DFT-MD (PBE) predictions of the first hydration shell around a number of transition-metal ions.[63] Numerical integration of this adsorbed water layer and the adjacent shoulder located at a height of ∼3−4 Å in the simulated structures gives a coverage of 2.06 O/A_{UC} for the PBE-based prediction and 2.04 O/A_{UC} for the PBE + Grimme-based prediction, in closer agreement with the value determined in the XR best fit (1.84 ± 0.12 O/A_{UC}). This suggests that DFT-MD successfully captures the amount of adsorbed water observed in the XR best fit, but the average height and vertical distribution of this water are quantitatively distinct. This leads to a smaller peak water density at the position of the first adsorbed layer, which largely explains the remaining discrepancies with the XR data.

The narrow width of the first adsorbed water layer observed in simulations compared to XR may be the result of our choice of DFT approximations. The PBE96 DFT GGA used in this work is computationally tractable, commonly used, and shown to provide a reliable and flexible description of interactions in solutions.[54,63] There are, however, well-documented problems with the accuracy of DFT approximations for the study of water interactions, and liquid water simulations have been shown to be sensitive to the integration parameters used to solve the Car−Parrinello equations. For example, in a study by Grossman et al.,[64] it was shown that liquid water was slightly over-structured (increased coordination/activity and slower self-diffusion rate) for choices of DFT and integration parameters similar to those used in our PBE simulations.

We note that the inclusion of dispersion corrections in our solvated surface simulations, i.e., PBE + Grimme,[35] had little effect on the over-structuring of liquid water at this interface. Other options, such as increasing the temperature of the simulation and using more recently developed exchange−correlation potentials,[65] should be explored to test how the level of DFT and integration parameters affect the adsorbed water width. There are, of course, always potential sources of systematic errors in experimental data (e.g., surface roughness, detector efficiency, sensitivity to the valence electron distribution) that would be expected primarily to impact the derived value of the rms width of an atomic layer rather than its position. These factors will need to be evaluated, especially when the simulations provide quantitative descriptions of the XR data.

4. DISCUSSION

The comparisons presented here highlight the benefits of directly pairing computational and experimental results. The initial visual comparison of the DFT-MD simulated density profiles showed the predictions were similar to the model obtained by model-dependent fitting of the XR data, although the quantitative agreement between the initial DFT-MD predictions and the XR data was unsatisfactory. Using the DFT-MD simulation as a starting point for optimization, we were able to achieve semiquantitative agreement by refining the initial predicted structures via comparison with XR data. Since the XR data analysis finds a local minimum based on a preconceived interface model and does not include explicit chemical constrains on the structural optimization, the present DFT-MD provides confidence that the best fit structure accurately represents the interfacial structure. This approach provides a route to identify and test other qualitatively different structures against the XR data.

The optimized DFT-MD-based structures (after optimizing the height but not the shape of the simulated water profiles, χ^2 = 6 and 7.6 for PBE and PBE + Grimme, respectively) did not quantitatively describe the XR data within the experimental uncertainties at the level of the model-dependent fit (χ^2 = 1.54), but they did result in a water layer height and a PBE-based alumina relaxation pattern in close agreement with the experimental observation (Figures 7 and S5). This provides confidence that the best fit water height and extended oscillatory alumina relaxation pattern are required by the XR data and are not artifacts of the starting model. In fact, this water height and relaxation behavior have been seen in previous analysis of XR measurements of the same system.[19] We suggest that residual discrepancies in Al_2O_3 surface displacements and the hydration structure are associated with very small energy differences, which underscores the importance of being able to identify sub-angstrom deviations between the DFT-MD and XR approaches. Such structural differences affect predictions of surface reactivity, as reflected in previous studies in which a ∼0.1 Å vertical displacement at the interface observed as a function of pH was associated with a change in protonation state due to an adsorbed hydroxyl vs a water molecule.[66]

4.1. Bulk Alumina Lattice Spacing. It is typical for PBE to underbind and consequently overestimate lattice constants, but the importance of this scaling issue has not been quantified previously. Although we find that the lattice mismatch between simulated and known alumina structures contributes significantly to disagreements with the XR data, this is expected due to the known sensitivity of X-ray scattering to bulk crystal structures. The 12-layer alumina slab used for this simulation still may have been insufficiently large for the slab to fully

DOI: 10.1021/acs.jpcc.8b08522
J. Phys. Chem. C 2018, 122, 26934−26944

converge to the known bulk structure, and more layers may be needed to achieve the known alumina bulk lattice constant. Nevertheless, the lattice was scaled here without affecting the interfacial structure, either alumina relaxation pattern or water structure. As such, this step does not affect the predictive value of DFT-MD. Since the pure PBE bulk calculation very accurately predicted the alumina lattice constants (within ~0.2%), the bulk lattice correction of the DFT-MD alumina slab may be performed based on the PBE DFT prediction without input from experimental XR data and before refinement of the DFT-MD interface structure, which is already common practice when comparing predicted crystal structures to experimental observation.

4.2. Interfacial Water Profile. The difference in the average first water layer height between ~2.53 Å from the XR data and 2.63−2.73 Å seen by DFT-MD may suggest a discrepancy in the interaction strength between the adsorbed water and the alumina terminal hydroxyls. We first discuss this difference in the context of the hydrogen bonding of water to the alumina surface. The XR-observed height would suggest an unusually short H-bond if the water was located directly above the surface oxygen. The average nearest neighbor oxygen distance is ~2.7−2.8 Å between H-bonded water molecules.[67,68] However, the specular XR measurements presented probe only the projection of O−O "bonds" along the alumina (001) surface normal direction. Assuming a bulklike H-bond O−O distance of 2.7 Å, the water height of 2.53 Å is consistent with a water adsorption site that is laterally displaced by ~1 Å on average from the alumina surface oxygen site. Off-specular XR measurements can directly probe the lateral water organization but were not done. However, one might expect this kind of lateral displacement of water adsorbed to alumina based on similar findings of adsorbed water on the isostructural α-Fe_2O_3(001) surface. In that case, the vertical height of adsorbed water was 1.9 Å,[19] and off-specular XR revealed a lateral displacement of water molecules from adjacent surface OH groups of ~1.8 Å,[69] consistent with a typical H-bonded OH−O distance.

A snapshot of the lateral water organization from the PBE-based simulation supports this hypothesis and reveals that the adsorbed water is primarily adsorbed near the alumina surface oxygen, but with a visible lateral shift, as seen in Figure 8a. A more quantitative assessment of this behavior can be obtained from the simulated radial distribution functions (RDF) between the surface O and the nearest neighbor water O, averaged over all snapshots in the respective DFT-MD simulations. These RDFs show an O−O separation of ~2.9 Å for the PBE-based DFT-MD and ~2.8 Å for the PBE + Grimme-based DFT-MD simulation (Figure 8b). The combination of the observed average vertical water layer heights and the RDFs suggests an average lateral displacement of adsorbed water relative to alumina surface oxygen sites of ~1 Å for both simulations, consistent with that inferred by XR with the assumption of a bulklike O−O H-bond length. This suggests that the primary disagreement between DFT-MD and XR in the average adsorbed water vertical height appears to derive from a longer than expected O−O separation in the DFT-MD simulations, especially in the case of the PBE-based DFT-MD. This predicted longer O−O distance would suggest that the H-bond interactions between the alumina surface and adsorbed water is weaker in the simulation compared to what is inferred from the experimental data.

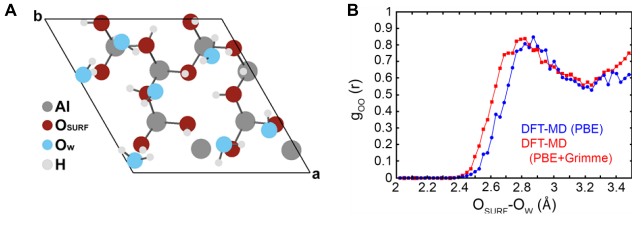

Figure 8. (A) Snapshot of the in-plane alumina (001) unit cell ($a \times b$) from the PBE DFT-MD simulation reveals the water oxygen (O_w) adsorption sites (pale blue) relative to the alumina surface oxygens (O_{surf}, red). (B) Radial distribution functions (normalized to the unit cell volume, V_{UC}) for the PBE and PBE + Grimme DFT-MD calculations show nearest neighbor distances between O_{surf} and O_w of ~2.9 and ~2.8 Å, respectively.

Another potential source of discrepancy between the simulated and measured water structures derives from the specific protonation state of the surface. The differences in the water heights seen here are similar to those observed previously at the TiO_2(110)/water interface that were associated with changes of the surface charge and proton site distributions.[70] The results here imply that differences in the adsorbed proton coverage on the experimental surface with respect to that in the DFT-MD simulations (i.e., one proton per surface oxygen) may be an additional source of discrepancy, such as might be expected from a pH-dependent surface charge with a point-of-zero below pH = 7. One might reasonably expect that such a change in surface charge would lead to a slightly stronger H-bond, as inferred here for the XR best fit relative to the DFT-MD predictions. Although the point-of-zero charge for alumina occurs at a pH of 6−8, SFG studies of this system showed a subtle change in spectral response between a pH of 6 and 8,[15] which may be consistent with a slight change in the surface charge. These behaviors can be explored with additional XR and DFT-MD studies of the pH dependence of the interfacial water structure to determine how the assumption of a charge-neutral surface or the choice of functional contributes to the predicted O−O distances. Nevertheless, the integrated comparison of DFT-MD with XR data has identified residual discrepancies in the combined accuracy of these approaches and provides a pathway for resolving these issues.

4.3. Choice of DFT Functional. The present results were performed with a single, well-known, and commonly used DFT exchange−correlation functional, PBE96, but there are many DFT functionals and corrections[35,41,71−75] with distinct strengths and weaknesses. Here, a DFT-MD simulation using the Grimme2 correction was used to assess whether the incorporation of a phenomenological correction for H-bonding would improve agreement. Inclusion of the Grimme correction changed the interfacial H-bonding, leading to a closer H-bond O−O distance of 2.8 Å between surface hydroxyls and water compared to the value from the PBE DFT-MD of 2.9 Å. However, optimization of the DFT-MD simulation with the Grimme correction (including all aspects of the structure except for the shape of the interfacial water profile) ultimately resulted in slightly worse agreement with the experimental XR data (χ^2 = 7.6 vs PBE χ^2 = 6). This is because the shape of the simulated interfacial water profile was less consistent with the XR data than the water profile obtained in the DFT-MD simulation using PBE alone. Grimme corrects for long-range energetics and is known to give a more correct density of water than PBE,[76] but it does not capture midrange interactions.

DOI: 10.1021/acs.jpcc.8b08522
J. Phys. Chem. C 2018, 122, 26934−26944

Namely, the PBE + Grimme structure showed a first adsorbed water layer with an even smaller coverage and width than that in the PBE DFT-MD calculation (Figure 7 and Table S1). In the end, neither simulation was able to capture the full details of the chemical environment seen in the experiment.

Comparison with other DFT functionals can be used to assess whether better agreement can be achieved for the alumina/water structure. For example, PBE0 using exact exchange may resolve some of the sub-angstrom discrepancies with the experimental best fit structure observed here, but it is not expected to improve significantly the quantitative level of agreement with the XR data. PBE0 has only offered limited improvement in similar systems, i.e., hydrated cation species[63] and the goethite−water interface,[58] at substantial added cost. The incorporation of van der Waals (vdW) interactions into DFT functionals is an active area of study and has been shown to improve the structure and dynamics of bulk water.[35] For example, the recently developed SCAN functional[74] incorporates an improved description of weak interactions, including H-bonding and vdW relative to PBE, and overall has performed remarkably well for bulk water at a similar cost to PBE.[75]

5. CONCLUSIONS

This study shows how quantitative comparisons of XR and DFT-MD simulations can evaluate the accuracy of our understanding of a simple, well-defined structure: the Al_2O_3(001)/water interface (i.e., including the substrate relaxation and interfacial water density profiles). The DFT-MD predicted structures give good visual agreement to the structures determined by the experimental best fit, showing that the PBE-based simulations are able to qualitatively capture many physiochemical behaviors at this interface. However, significant quantitative differences between the measured XR signals and those calculated based on the DFT-MD simulations demonstrate sub-angstrom differences between predicted structures and experimental data. For example, differences in the oscillatory relaxation behavior of atoms in the top four alumina layers and the effective bulk alumina lattice constant (i.e., in the center of the simulated slab) are observed. These differences appear not to be converged in the DFT-MD simulations despite the large alumina slab size used. The differences are, however, similar in magnitude to the small discrepancy between the known alumina lattice constant and that calculated in a bulk PBE calculation, suggesting that these differences may be within the accuracy of these electronic structure calculations.

The small but significant changes to the bulk and interfacial simulated DFT-MD structures accentuate the deep structural insights that can ultimately be derived from these comparisons. For example, we observe differences in the adsorbed water structure and hypothesize that differences between experiment and computation may be explained, at least in part, by the protonation state at the interface. This may have implications for DFT-MD-predicted HB networks and proton-transfer dynamics at the interface. Calculations that include both mid- and long-range interactions and ones that test effects of surface protonation state are needed to answer questions raised by this discrepancy and to fully understand the water interactions with the alumina surface. Finally, this study paves the way for future DFT-MD−XR analyses of other systems to refine predicted structures and to provide a starting point for XR data analysis of more complex systems without the need for a preconceived model of the interface.

■ ASSOCIATED CONTENT

Supporting Information

The Supporting Information is available free of charge on the ACS Publications website at DOI: 10.1021/acs.jpcc.8b08522.

Al_2O_3 crystal structure; DFT-MD calculation core radii; DFT-MD incorporation into XR analysis and structure optimization including residuals; optimization and results (PDF)

■ AUTHOR INFORMATION

Corresponding Author

*E-mail: fenter@anl.gov.

ORCID

Katherine J. Harmon: 0000-0001-6427-7971
Michael J. Bedzyk: 0000-0002-1026-4558
Paul Fenter: 0000-0002-6672-9748

Notes

The authors declare no competing financial interest.

■ ACKNOWLEDGMENTS

This work was supported by the U.S. Department of Energy, Office of Basic Energy Sciences (DOE/BES) Division of Chemical Sciences, Geosciences, and Biosciences (Geosciences Research Program) through Argonne National Laboratory (ANL), the University of California San Diego, and Pacific Northwest National Laboratory. K.J.H. gratefully acknowledges support from the Department of Defense (DoD) through the National Defense Science & Engineering Graduate Fellowship (NDSEG) Program and from the Ryan Fellowship and the Northwestern University International Institute for Nanotechnology. J.G.C. was supported by the U.S. National Science Foundation (NSF) Environmental Chemical Sciences Program (Award No. CHE-1505532). Additional support from EMSL operations. EMSL operations are supported by the DOE's Office of Biological and Environmental Research (Contract number DE-AC06-76RLO 1830). We wish to thank the Scientific Computing Staff, Office of Energy Research, and the U. S. Department of Energy for a grant of computer time at the National Energy Research Scientific Computing Center (Berkeley, CA). Some of the calculations were performed on the Cascade computing systems at the Molecular Science Computing Facility in the William R. Wiley Environmental Molecular Sciences Laboratory (EMSL) at PNNL. X-ray reflectivity measurements were performed at beamline 33-ID-D of the Advanced Photon Source at ANL, a U.S. DOE Office of Science User Facility operated by ANL under Contract No. DE-AC02-06CH11357. The submitted manuscript has been created by UChicago Argonne, LLC, Operator of Argonne National Laboratory ("Argonne"). Argonne, a U.S. Department of Energy Office of Science laboratory, is operated under Contract No. DE-AC02-06CH11357. The U.S. Government retains for itself, and others acting on its behalf, a paid-up nonexclusive, irrevocable worldwide license in said article to reproduce, prepare derivative works, distribute copies to the public, and perform publicly and display publicly, by or on behalf of the Government. The Department of Energy will provide public access to these results of federally sponsored research in

DOI: 10.1021/acs.jpcc.8b08522
J. Phys. Chem. C 2018, 122, 26934−26944

accordance with the DOE Public Access Plan. http://energy.gov/downloads/doe-public-accessplan.

REFERENCES

(1) Wieland, E.; Wehrli, B.; Stumm, W. The Coordination Chemistry of Weathering: III. A Generalization on the Dissolution Rates of Minerals. *Geochim. Cosmochim. Acta* **1988**, *52*, 1969−1981.

(2) Wagner, F. T.; Somorjai, G. A. Photocatalytic and Photoelectrochemical Hydrogen Production on Strontium Titanate Single Crystals. *J. Am. Chem. Soc.* **1980**, *102*, 5494−5502.

(3) Park, E. D.; Choi, S. H.; Lee, J. S. Active States of Pd and Cu in Carbon-Supported Wacker-Type Catalysts for Low-Temperature CO Oxidation. *J. Phys. Chem. B* **2000**, *104*, 5586−5594.

(4) Stamenkovic, V. R.; Fowler, B.; Mun, B. S.; Wang, G.; Ross, P. N.; Lucas, C. A.; Marković, N. M. Improved Oxygen Reduction Activity on $Pt_3Ni(111)$ via Increased Surface Site Availability. *Science* **2007**, *315*, 493−497.

(5) Fuller, C. C.; Davis, J. A.; Waychunas, G. A. Surface Chemistry of Ferrihydrite: Part 2. Kinetics of Arsenate Adsorption and Coprecipitation. *Geochim. Cosmochim. Acta* **1993**, *57*, 2271−2282.

(6) Catalano, J. G.; Trainor, T. P.; Eng, P. J.; Waychunas, G. A.; Brown, G. E. CTR Diffraction and Grazing-Incidence EXAFS Study of U(VI) Adsorption onto α-Al_2O_3 and α-Fe_2O_3 $(1\bar{1}02)$ Surfaces. *Geochim. Cosmochim. Acta* **2005**, *69*, 3555−3572.

(7) Lee, S. S.; Fenter, P.; Park, C.; Sturchio, N. C.; Nagy, K. L. Hydrated Cation Speciation at the Muscovite (001)−Water Interface. *Langmuir* **2010**, *26*, 16647−16651.

(8) Fernandez-Martinez, A.; Hu, Y.; Lee, B.; Jun, Y.-S.; Waychunas, G. A. In Situ Determination of Interfacial Energies between Heterogeneously Nucleated $CaCO_3$ and Quartz Substrates: Thermodynamics of CO_2 Mineral Trapping. *Environ. Sci. Technol.* **2013**, *47*, 102−109.

(9) Lindgren, T.; Wang, H.; Beermann, N.; Vayssieres, L.; Hagfeldt, A.; Lindquist, S.-E. Aqueous Photoelectrochemistry of Hematite Nanorod Array. *Sol. Energy Mater. Sol. Cells* **2002**, *71*, 231−243.

(10) Sivula, K.; Le Formal, F.; Grätzel, M. Solar Water Splitting: Progress Using Hematite (α-Fe_2O_3) Photoelectrodes. *ChemSusChem* **2011**, *4*, 432−449.

(11) Shen, Y. R.; Ostroverkhov, V. Sum-Frequency Vibrational Spectroscopy on Water Interfaces: Polar Orientation of Water Molecules at Interfaces. *Chem. Rev.* **2006**, *106*, 1140−1154.

(12) Zhang, L.; Tian, C.; Waychunas, G. A.; Shen, Y. R. Structures and Charging of α-Alumina (0001)/Water Interfaces Studied by Sum-Frequency Vibrational Spectroscopy. *J. Am. Chem. Soc.* **2008**, *130*, 7686−7694.

(13) Boulesbaa, A.; Borguet, E. Vibrational Dynamics of Interfacial Water by Free Induction Decay Sum Frequency Generation (FID-SFG) at the $Al_2O_3(1120)/H_2O$ Interface. *J. Phys. Chem. Lett.* **2014**, *5*, 528−533.

(14) Tuladhar, A.; Dewan, S.; Kubicki, J. D.; Borguet, E. Spectroscopy and Ultrafast Vibrational Dynamics of Strongly Hydrogen Bonded OH Species at the α-$Al_2O_3(11\bar{2}0)/H_2O$ Interface. *J. Phys. Chem. C* **2016**, *120*, 16153−16161.

(15) Tuladhar, A.; Piontek, S. M.; Borguet, E. Insights on Interfacial Structure, Dynamics, and Proton Transfer from Ultrafast Vibrational Sum Frequency Generation Spectroscopy of the Alumina(0001)/Water Interface. *J. Phys. Chem. C* **2017**, *121*, 5168−5177.

(16) Trainor, T. P.; Chaka, A. M.; Eng, P. J.; Newville, M.; Waychunas, G. A.; Catalano, J. G.; Brown, G. E. Structure and Reactivity of the Hydrated Hematite (0001) Surface. *Surf. Sci.* **2004**, *573*, 204−224.

(17) Catalano, J. G.; Park, C.; Zhang, Z.; Fenter, P. Termination and Water Adsorption at the α-Al_2O_3 (012)−Aqueous Solution Interface. *Langmuir* **2006**, *22*, 4668−4673.

(18) Catalano, J. G. Relaxations and Interfacial Water Ordering at the Corundum (110) Surface. *J. Phys. Chem. C* **2010**, *114*, 6624−6630.

(19) Catalano, J. G. Weak Interfacial Water Ordering on Isostructural Hematite and Corundum (001) Surfaces. *Geochim. Cosmochim. Acta* **2011**, *75*, 2062−2071.

(20) Lee, S. S.; Fenter, P.; Nagy, K. L.; Sturchio, N. C. Monovalent Ion Adsorption at the Muscovite (001)−Solution Interface: Relationships Among Ion Coverage and Speciation, Interfacial Water Structure, and Substrate Relaxation. *Langmuir* **2012**, *28*, 8637−8650.

(21) Uysal, A.; Chu, M.; Stripe, B.; Timalsina, A.; Chattopadhyay, S.; Schlepütz, C. M.; Marks, T. J.; Dutta, P. What X-rays Can Tell Us About the Interfacial Profile of Water Near Hydrophobic Surfaces. *Phys. Rev. B* **2013**, *88*, No. 035431.

(22) Fenter, P.; Zapol, P.; He, H.; Sturchio, N. C. On the Variation of Dissolution Rates at the Orthoclase (0 0 1) Surface with pH and Temperature. *Geochim. Cosmochim. Acta* **2014**, *141*, 598−611.

(23) Eng, P. J.; Trainor, T. P.; Brown, G. E., Jr.; Waychunas, G. A.; Newville, M.; Sutton, S. R.; Rivers, M. L. Structure of the Hydrated α-Al_2O_3 (0001) Surface. *Science* **2000**, *288*, 1029−1033.

(24) Marx, D.; Hutter, J. *Ab Initio Molecular Dynamics: Basic Theory and Advanced Methods*; Cambridge University Press, 2009.

(25) von Rudorff, G. F.; Jakobsen, R.; Rosso, K. M.; Blumberger, J. Fast Interconversion of Hydrogen Bonding at the Hematite (001)−Liquid Water Interface. *J. Phys. Chem. Lett.* **2016**, *7*, 1155−1160.

(26) Wan, Q.; Galli, G. First-Principles Framework to Compute Sum-Frequency Generation Vibrational Spectra of Semiconductors and Insulators. *Phys. Rev. Lett.* **2015**, *115*, No. 246404.

(27) DelloStritto, M.; Sofo, J. Bond Polarizability Model for Sum Frequency Generation at the $Al_2O_3(0001)-H_2O$ Interface. *J. Phys. Chem. A* **2017**, *121*, 3045−3055.

(28) Pezzotti, S.; Galimberti, D. R.; Shen, Y. R.; Gaigeot, M.-P. Structural Definition of the BIL and DL: A New Universal Methodology to Rationalize Non-Linear $\chi^{(2)}(\omega)$ SFG Signals at Charged Interfaces, Including $\chi^{(3)}(\omega)$ Contributions. *Phys. Chem. Chem. Phys.* **2018**, *20*, 5190−5199.

(29) Huang, P.; Pham, T. A.; Galli, G.; Schwegler, E. Alumina-(0001)/Water Interface: Structural Properties and Infrared Spectra from First-Principles Molecular Dynamics Simulations. *J. Phys. Chem. C* **2014**, *118*, 8944−8951.

(30) Gaigeot, M.-P.; Sprik, M.; Sulpizi, M. Oxide/Water Interfaces: How the Surface Chemistry Modifies Interfacial Water Properties. *J. Phys.: Condens. Matter* **2012**, *24*, No. 124106.

(31) Fenter, P.; Kerisit, S.; Raiteri, P.; Gale, J. D. Is the Calcite−Water Interface Understood? Direct Comparisons of Molecular Dynamics Simulations with Specular X-ray Reflectivity Data. *J. Phys. Chem. C* **2013**, *117*, 5028−5042.

(32) Bracco, J. N.; Lee, S. S.; Stubbs, J. E.; Eng, P. J.; Heberling, F.; Fenter, P.; Stack, A. G. Hydration Structure of the Barite (001)−Water Interface: Comparison of X-ray Reflectivity with Molecular Dynamics Simulations. *J. Phys. Chem. C* **2017**, *121*, 12236−12248.

(33) Perdew, J. P.; Burke, K.; Ernzerhof, M. Generalized Gradient Approximation Made Simple. *Phys. Rev. Lett.* **1996**, *77*, 3865−3868.

(34) Lejaeghere, K.; Bihlmayer, G.; Björkman, T.; Blaha, P.; Blügel, S.; Blum, V.; Caliste, D.; Castelli, I. E.; Clark, S. J.; Dal Corso, A.; et al. Reproducibility in Density Functional Theory Calculations of Solids. *Science* **2016**, *351*, No. aad3000.

(35) Gillan, M. J.; Alfè, D.; Michaelides, A. Perspective: How Good is DFT for Water? *J. Chem. Phys.* **2016**, *144*, No. 130901.

(36) Adamo, C.; Barone, V. Toward Reliable Density Functional Methods Without Adjustable Parameters: The PBE0 model. *J. Chem. Phys.* **1999**, *110*, 6158−6170.

(37) Chen, Y.; Bylaska, E.; Weare, J. First Principles Estimation of Geochemically Important Transition Metal Oxide Properties. In *Molecular Modeling of Geochemical Reactions: An Introduction*; John Wiley & Sons, 2016; pp 107−134.

(38) Argyris, D.; Ho, T.; Cole, D. R.; Striolo, A. Molecular Dynamics Studies of Interfacial Water at the Alumina Surface. *J. Phys. Chem. C* **2011**, *115*, 2038−2046.

(39) Hass, K. C.; Schneider, W. F.; Curioni, A.; Andreoni, W. The Chemistry of Water on Alumina Surfaces: Reaction Dynamics from First Principles. *Science* **1998**, *282*, 265−268.

DOI: 10.1021/acs.jpcc.8b08522
J. Phys. Chem. C 2018, 122, 26934−26944

(40) Hass, K. C.; Schneider, W. F.; Curioni, A.; Andreoni, W. First-Principles Molecular Dynamics Simulations of H_2O on α-Al_2O_3 (0001). *J. Phys. Chem. B* **2000**, *104*, 5527−5540.
(41) Grimme, S. Semiempirical GGA-Type Density Functional Constructed with a Long-Range Dispersion Correction. *J. Comput. Chem.* **2006**, *27*, 1787−1799.
(42) Grimme, S.; Antony, J.; Ehrlich, S.; Krieg, H. A Consistent and Accurate Ab Initio Parametrization of Density Functional Dispersion Correction (DFT-D) for the 94 Elements H-Pu. *J. Chem. Phys.* **2010**, *132*, No. 154104.
(43) Bylaska, E.; Tsemekhman, K.; Govind, N.; Valiev, M. Large-Scale Plane-Wave-Based Density Functional Theory: Formalism, Parallelization, and Applications. In *Computational Methods for Large Systems: Electronic Structure Approaches for Biotechnology and Nanotechnology*; Wiley, 2011; pp 77−116.
(44) Bylaska, E. J. Plane-Wave DFT Methods for Chemistry. In *Annual Reports in Computational Chemistry*; Elsevier, 2017; Vol. *13*, pp 185−228.
(45) Valiev, M.; Bylaska, E. J.; Govind, N.; Kowalski, K.; Straatsma, T. P.; Van Dam, H. J.; Wang, D.; Nieplocha, J.; Apra, E.; Windus, T. L.; de Jong, W. A. NWChem: A Comprehensive and Scalable Open-Source Solution for Large Scale Molecular Simulations. *Comput. Phys. Commun.* **2010**, *181*, 1477−1489.
(46) Monkhorst, H. J.; Pack, J. D. Special Points for Brillouin-Zone Integrations. *Phys. Rev. B* **1976**, *13*, 5188−5192.
(47) Hamann, D. Generalized Norm-Conserving Pseudopotentials. *Phys. Rev. B* **1989**, *40*, 2980−2987.
(48) Hamann, D.; Schlüter, M.; Chiang, C. Norm-Conserving Pseudopotentials. *Phys. Rev. Lett.* **1979**, *43*, 1494−1497.
(49) Kleinman, L.; Bylander, D. M. Efficacious Form for Model Pseudopotentials. *Phys. Rev. Lett.* **1982**, *48*, 1425−1428.
(50) Bylaska, E. J.; Valiev, M.; Rustad, J. R.; Weare, J. H. Structure and Dynamics of the Hydration Shells of the Al3+ Ion. *J. Chem. Phys.* **2007**, *126*, No. 104505.
(51) Kondo, S.; Tateishi, K.; Ishizawa, N. Structural Evolution of Corundum at High Temperatures. *Jpn. J. Appl. Phys.* **2008**, *47*, 616−619.
(52) Car, R.; Parrinello, M. Unified Approach for Molecular Dynamics and Density-Functional Theory. *Phys. Rev. Lett.* **1985**, *55*, 2471−2474.
(53) Fenter, P.; Lee, S. S. Hydration Layer Structure at Solid−Water Interfaces. *MRS Bull.* **2014**, *39*, 1056−1061.
(54) Cauët, E.; Bogatko, S.; Weare, J. H.; Fulton, J. L.; Schenter, G. K.; Bylaska, E. J. Structure and Dynamics of the Hydration Shells of the Zn2+ Ion from Ab Initio Molecular Dynamics and Combined Ab Initio and Classical Molecular Dynamics Simulations. *J. Chem. Phys.* **2010**, *132*, No. 194502.
(55) Nosé, S. A Unified Formulation of the Constant Temperature Molecular Dynamics Methods. *J. Chem. Phys.* **1984**, *81*, 511−519.
(56) Hoover, W. G. Canonical Dynamics: Equilibrium Phase-Space Distributions. *Phys. Rev. A* **1985**, *31*, 1695−1697.
(57) Blöchl, P. E.; Parrinello, M. Adiabaticity in First-Principles Molecular Dynamics. *Phys. Rev. B* **1992**, *45*, 9413−9416.
(58) Chen, Y.; Bylaska, E. J.; Weare, J. H. Weakly Bound Water Structure, Bond Valence Saturation and Water Dynamics at the Goethite (100) Surface/Aqueous Interface: Ab Initio Dynamical Simulations. *Geochem. Trans.* **2017**, *18*, No. 3.
(59) Magnussen, O. M.; Ocko, B. M.; Regan, M. J.; Penanen, K.; Pershan, P. S.; Deutsch, M. X-Ray Reflectivity Measurements of Surface Layering in Liquid Mercury. *Phys. Rev. Lett.* **1995**, *74*, 4444−4447.
(60) Robinson, I. K. Crystal Truncation Rods and Surface Roughness. *Phys. Rev. B* **1986**, *33*, 3830−3836.
(61) Fenter, P.; Lee, S. S.; Skelton, A. A.; Cummings, P. T. Direct and Quantitative Comparison of Pixelated Density Profiles with High-Resolution X-ray Reflectivity Data. *J. Synchrotron Radiat.* **2011**, *18*, 257−265.
(62) Herbstein, F. How Precise are Measurements of Unit-Cell Dimensions from Single Crystals? *Acta Crystallogr., Sect. B: Struct. Sci., Cryst. Eng. Mater.* **2000**, *56*, 547−557.
(63) Fulton, J. L.; Bylaska, E. J.; Bogatko, S.; Balasubramanian, M.; Cauët, E.; Schenter, G. K.; Weare, J. H. Near-Quantitative Agreement of Model-Free DFT-MD Predictions with XAFS Observations of the Hydration Structure of Highly Charged Transition-Metal Ions. *J. Phys. Chem. Lett.* **2012**, *3*, 2588−2593.
(64) Grossman, J. C.; Schwegler, E.; Draeger, E. W.; Gygi, F.; Galli, G. Towards an Assessment of the Accuracy of Density Functional Theory for First Principles Simulations of Water. *J. Chem. Phys.* **2004**, *120*, 300−311.
(65) Sun, J.; Remsing, R. C.; Zhang, Y.; Sun, Z.; Ruzsinszky, A.; Peng, H.; Yang, Z.; Paul, A.; Waghmare, U.; Wu, X.; et al. Accurate First-Principles Structures and Energies of Diversely Bonded Systems from an Efficient Density Functional. *Nat. Chem.* **2016**, *8*, 831−836.
(66) Zhang, Z.; Fenter, P.; Sturchio, N. C.; Bedzyk, M. J.; Machesky, M. L.; Wesolowski, D. J. Structure of Rutile TiO_2 (110) in Water and 1 Molal Rb+ at pH 12: Inter-Relationship Among Surface Charge, Interfacial Hydration Structure, and Substrate Structural Displacements. *Surf. Sci.* **2007**, *601*, 1129−1143.
(67) Bergmann, U.; Cicco, A. D.; Wernet, P.; Principi, E.; Glatzel, P.; Nilsson, A. Nearest-Neighbor Oxygen Distances in Liquid Water and Ice Observed by X-ray Raman Based Extended X-ray Absorption Fine Structure. *J. Chem. Phys.* **2007**, *127*, No. 174504.
(68) Hura, G.; Sorenson, J. M.; Glaeser, R. M.; Head-Gordon, T. A High-Quality X-ray Scattering Experiment on Liquid Water at Ambient Conditions. *J. Chem. Phys.* **2000**, *113*, 9140−9148.
(69) Tanwar, K. S.; Petitto, S. C.; Ghose, S. K.; Eng, P. J.; Trainor, T. P. Fe(II) Adsorption on Hematite (0001). *Geochim. Cosmochim. Acta* **2009**, *73*, 4346−4365.
(70) Zhang, Z.; Fenter, P.; Cheng, L.; Sturchio, N. C.; Bedzyk, M. J.; Předota, M.; Bandura, A.; Kubicki, J. D.; Lvov, S. N.; Cummings, P. T.; et al. Ion Adsorption at the Rutile−Water Interface: Linking Molecular and Macroscopic Properties. *Langmuir* **2004**, *20*, 4954−4969.
(71) Heyd, J.; Scuseria, G. E.; Ernzerhof, M. Hybrid Functionals Based on a Screened Coulomb Potential. *J. Chem. Phys.* **2003**, *118*, 8207−8215.
(72) Klimeš, J.; Bowler, D. R.; Michaelides, A. Van der Waals Density Functionals Applied to Solids. *Phys. Rev. B* **2011**, *83*, No. 195131.
(73) Brandenburg, J. G.; Maas, T.; Grimme, S. Benchmarking DFT and Semiempirical Methods on Structures and Lattice Energies for Ten Ice Polymorphs. *J. Chem. Phys.* **2015**, *142*, No. 124104.
(74) Sun, J.; Ruzsinszky, A.; Perdew, J. P. Strongly Constrained and Appropriately Normed Semilocal Density Functional. *Phys. Rev. Lett.* **2015**, *115*, No. 036402.
(75) Chen, M.; Ko, H.-Y.; Remsing, R. C.; Calegari Andrade, M. F.; Santra, B.; Sun, Z.; Selloni, A.; Car, R.; Klein, M. L.; Perdew, J. P.; et al. Ab Initio Theory and Modeling of Water. *Proc. Natl. Acad. Sci. U.S.A.* **2017**, *114*, 10846−10851.
(76) Lin, I. C.; Seitsonen, A. P.; Tavernelli, I.; Rothlisberger, U. Structure and Dynamics of Liquid Water from ab Initio Molecular Dynamics—Comparison of BLYP, PBE, and revPBE Density Functionals with and Without van der Waals Corrections. *J. Chem. Theory Comput.* **2012**, *8*, 3902−3910.

DOI: 10.1021/acs.jpcc.8b08522
J. Phys. Chem. C 2018, 122, 26934−26944